High-mobility and High-reliability Zn-incorporated Amorphous In_2O_3-based Thin-Film Transistors

Yuzhang Wu[1], Yusaku Magari[2,*], Prashant R. Ghediya[2], Yuqiao Zhang[3], Yasutaka Matsuo[2], and Hiromichi Ohta[2,*]

[1] *Graduate School of Information Science and Technology, Hokkaido University, N14W9, Sapporo 060-0814, Japan*
[2] *Research Institute for Electronic Science, Hokkaido University, N20W10, Sapporo 001-0020, Japan*
[3] *Institute of Quantum and Sustainable Technology, Jiangsu University, Zhenjiang 212013, China*
*Email: magari.yusaku@es.hokudai.ac.jp, hiromichi.ohta@es.hokudai.ac.jp

Polycrystalline indium oxide-based thin film transistors (In_2O_3 TFTs) have attracted considerable attention because of high field effect mobility (μ_{FE} ~100 cm^2 V^{-1} s^{-1}). However, In_2O_3 TFTs exhibit poor reliability owing to the adsorption and/or desorption of gas molecules at the grain boundaries. The incorporation of Zn suppresses the crystallization of In_2O_3. Herein, we systematically studied the effect of Zn incorporation into In_2O_3 TFTs. The crystallization of In_2O_3 was suppressed when the Zn concentration ranging from 25% to 68%. Amorphous IZO TFTs with 25% Zn exhibited the highest μ_{FE} of 41 cm^2 V^{-1} s^{-1} and excellent reliability. In contrast, polycrystalline IZO TFTs showed a low μ_{FE} <12 cm^2 V^{-1} s^{-1} due to the formation of grain boundaries, and poor reliability after positive gate bias, mostly due to electron trapping at the polycrystalline/insulator interface. These results render an approach to realize In_2O_3 TFTs that show reasonably high μ_{FE} and excellent reliability.

1. Introduction

Transparent oxide semiconductor (TOS)-based thin-film transistors (TFTs), represented by amorphous $InGaZnO_4$ TFTs, have been widely employed as the backplanes of active-matrix flat-panel displays of OLED and LCD TVs. Since amorphous $InGaZnO_4$ TFTs exhibit one or two orders of magnitude higher field-effect mobility (μ_{FE} ~10 cm^2 V^{-1} s^{-1}) than that of previously used amorphous Si TFTs (μ_{FE} ~0.5 cm^2 V^{-1} s^{-1}), 4 K

definition displays (3840 × 2160 pixels) with a frequency of 240 Hz single scan have been realized.[1-4] In the future, with an increasing demand for higher-definition display (8 K with 7680 × 4320 pixels) with high frequencies (480 Hz, single scan), TOS-TFTs that exhibit higher μ_{FE} (>50 $cm^2 V^{-1} s^{-1}$) would be required for pixel-driving circuits.[5-8]

Among numerous reports on TOS-TFTs showing higher μ_{FE} (> 50 $cm^2 V^{-1} s^{-1}$), In_2O_3 TFTs are considered a promising candidate because of their high field effect mobility (μ_{FE} ~100 $cm^2 V^{-1} s^{-1}$).[9] However, they suffer from the following serious drawbacks: In_2O_3 TFTs typically show poor reliability, especially after applying negative gate bias stress, owing to the adsorption and/or desorption of gas molecules at the grain boundaries.[9, 10] Notably, Zn incorporation suppresses the crystallization of In_2O_3.[11-19] Since $In_2O_3(ZnO)_m$ (m = integer) has a complicated layered structure, the crystallization does not occur at lower temperatures (<500 °C). Recently, Liang *et al.* reported that the 40% Zn-incorporated In_2O_3 TFT exhibited a high μ_{FE} of 53.6 $cm^2 V^{-1} s^{-1}$.[20] However, the effects of Zn addition to In_2O_3 on the electrical properties and crystal structure of IZO films, as well as on the TFT characteristics and reliability, have not been thoroughly understood.

Herein, we systematically studied the effect of Zn incorporation into In_2O_3 TFTs using Zn-incorporated In_2O_3 (IZO) thin films with various Zn concentrations. We found that the crystallization of In_2O_3 was suppressed when the Zn concentration was >25%, whereas the crystallization of ZnO occurred when the Zn concentration was >68%.

When the Zn concentration was in the range of 25%–68%, an amorphous structure was stabilized. Amorphous IZO TFTs with 25% Zn exhibited the highest μ_{FE} of 41 $cm^2 V^{-1} s^{-1}$ and excellent reliability. In contrast, polycrystalline IZO TFTs showed a low μ_{FE} <12 $cm^2 V^{-1} s^{-1}$ due to the formation of grain boundaries, and poor reliability after positive gate bias, mostly due to electron trapping at the polycrystalline/insulator interface. This study provides an approach to optimize In_2O_3 TFTs for high μ_{FE} and excellent reliability, to be useful for the further development of oxide TFTs.

2. Experimental methods

2.1 Fabrication of IZO films

IZO (10 wt.% ZnO added In_2O_3, $In_2O_3(ZnO)_m$, m = 1, 2, 9, and 20) targets were prepared using a conventional ceramic process for the deposition of IZO films. IZO films were fabricated on alkali-free glass substrates (EAGLE XG®, Corning®) by pulsed

laser deposition (PLD) method at 25 °C using a KrF excimer laser (~1.5 J cm^{-2} $pulse^{-1}$, 10 Hz). The oxygen pressure was maintained at 3 Pa during deposition. Typical deposition rate was ~0.3 nm s^{-1}. The Zn concentrations [atomic ratio of Zn/(Zn + In) ×100 (%)] of the resultant IZO films, measured using inductively coupled plasma mass spectrometry (ICP-MS), were 9%, 25%, 41%, 68%, and 86%. The Zn concentration in the resulting films differed slightly from the PLD target concentration. After the deposition, the IZO films were annealed at 300 °C in air for 0.5 h.

2.2 Structure analyses and electron transport properties measurements of the IZO films

The thickness, density, and surface roughness of the resultant IZO films were measured using X-ray reflectivity (XRR, ATX-G, Rigaku Co.). The X-ray diffraction (XRD) patterns of the resulting films were also measured. The incident angle of the X-rays was fixed at 0.5° while 2θ scanning was performed. The electrical resistivity (ρ), carrier concentration (n), and Hall mobility (μ_{Hall}) of the IZO thin films were measured by a DC four-probe method with a van der Pauw electrode configuration. Thermopower (S) was measured using a conventional steady-state method at 25 °C with laboratory-made equipment.[21, 22)]

2.3 Fabrication of IZO-TFTs

We fabricated IZO TFTs (bottom-gate & top-contact type) on alkaline-free glass substrates (EAGLE XG®, Corning®) as shown in **Fig. 1**. First, a 100-nm-thick AlO_x film, which served as the gate insulator, was deposited by atomic layer deposition (ALD) onto an indium tin oxide (ITO)-coated glass substrate. The dielectric permittivity (ε_r) and capacitance (C_i) of the AlO_x films were 8 and 70 nF cm^{-2}, respectively. Subsequently, 5-nm-thick IZO films with different Zn concentrations were deposited onto the AlO_x films via PLD under an oxygen pressure of 3 Pa at room temperature through a stencil mask. The multilayer film was annealed at 300 °C in ambient air for 0.5 h. Subsequently, 100-nm-thick ITO source/drain electrodes were deposited by PLD through a stencil mask. The channel length (L) and width (W) were 200 and 400 μm, respectively. Subsequently, a ~50-nm-thick Y_2O_3 film was deposited via PLD through a stencil mask without substrate heating. This film served as a passivation layer. Finally, the TFT was thermally annealed at 300 °C in air for 0.5 h.

3. Results and discussion

First, we fabricated the IZO films and analyzed their microstructures. **Figure 2** shows the

XRD patterns of the (a) as-deposited and (b) 300 °C annealed In_2O_3 (Zn = 0%) and IZO (Zn = 9%, 25%, 41%, 68%, and 86%) films. The In_2O_3 films, both with and without annealing, exhibited intense diffraction peaks, indicating their polycrystalline nature. This is consistent with previous reports in which In_2O_3 was crystallized at room temperature.[9] For Zn concentrations ranging from 25%−68%, a halo is seen at approximately $2\theta \sim 34°$, whereas the diffraction peaks appear for Zn concentrations of 9% and 86%. Thus, a moderate amount of Zn in IZO films (Zn%: 25%−68%) stabilizes the amorphous structure even after annealing at 300 °C. The IZO films with low (<25%) and high Zn (>68%) concentrations crystallized even at room temperature. In Zn-rich area, it should be noticed that though 68% Zn is higher than reported Zn ratio of polycrystalline IZO (50 at.%),[23] films still stay in amorphous phase. In In-rich area, the Zn ratio of 9% Zn films is well consistent with the reported crystallization of Zn ratio <16 wt.%.[24, 25]

Subsequently, we measured the electron transport properties of the IZO films. **Figure 3** shows changes in carrier concentration (n), Hall mobility (μ_{Hall}), and thermopower (S) as a function of Zn concentration in the IZO films. The n of as-deposited IZO films is high ($\sim 10^{20}$ cm^{-3} level) and decreases slightly with increasing Zn concentration, whereas it decreases significantly to $\sim 10^{17}$ cm^{-3} after annealing (**Fig. 3a**). This could be attributed to the significant suppression of oxygen deficiencies after annealing the amorphous IZO films. By contrast, the n values of the polycrystalline In_2O_3 and IZO film with 9% Zn do not suppress significantly as in the amorphous films. This phenomenon is probably owing to the adsorption of O^{2-} or OH^- ions at the grain boundaries that results in the formation of a double Schottky barrier instead of filling deficiencies.[26] The μ_{Hall} of the as-deposited films is in the range of 20−30 $cm^2\ V^{-1}\ s^{-1}$ regardless of the Zn concentration (**Fig. 3b**). After annealing at 300 °C, In_2O_3 film exhibited the highest μ_{Hall} of 22.2 $cm^2\ V^{-1}\ s^{-1}$. In general, the grain boundaries have a relatively small impact on μ_{Hall} in transparent conductive oxides with high n ($>10^{19}$ cm^{-3}) because electrons can tunnel through the narrow width.[27] The μ_{Hall} of the 9% Zn film significantly decreased (6.4 $cm^2\ V^{-1}\ s^{-1}$) after annealing due to grain boundary scattering caused by the reduction in n.

The μ_{Hall} of the amorphous IZO films decreases gradually after annealing with increasing Zn concentration. To understand the carrier electron transport properties in detail, we measured the S of the IZO films (**Fig. 3c**) because S does not strongly reflect the film quality compared to electron mobility. The $|S|$ of the as-deposited films is small (<50 $\mu V\ K^{-1}$) because of the high carrier concentration of the films. After the annealing, the $|S|$ of the amorphous IZO films increases (> 400 $\mu V\ K^{-1}$), reflecting their low carrier

concentration (~10^{17} cm^{-3}).

S reflects the energy differential of the density of states at the Fermi energy, providing an estimate of carrier effective mass (m^*) of materials.[28-30] m^* is inversely proportional to the mobility ($\mu = e \cdot \tau \cdot m^{*-1}$, where e and τ are the electron charge and carrier relaxation time, respectively). **Figure 4a** shows the *S* values of the IZO films as a function of *n* (log scale) at room temperature. From the relationship between *n* and *S*, the carrier effective mass (m^*) can be determined using the following equations:[28]

$$n_{3D} = 4\pi \left(\frac{2.m_d^*.k_B.T}{h^2}\right)^{1.5} F_r(\xi), \qquad \text{(Equation 1)}$$

$$F_r(\xi) = \int_0^\infty \frac{x^r}{1+e^{x-\xi}} dx, \qquad \text{(Equation 2)}$$

$$S = -\frac{k_B}{e}\left(\frac{(r+2)F_{r+1}(\xi)}{(r+1)F_r(\xi)} - \xi\right), \qquad \text{(Equation 3)}$$

where m_d^*, k_B, T, h, ξ, F_r, and r are the density of states effective mass (m_d^* = spin degeneracy × m^* = $2m^*$), Boltzmann constant, absolute temperature, Planck constant, chemical potential, Fermi integral, and scattering parameter of the relaxation time, respectively. The observed *S* is well-fitted with the calculated m_0 line in the range of 0.1−0.2 m_0, regardless of the Zn concentration. For IZO with a Zn concentration of 86%, *S* is lower than the corresponded simulating value of the linear correlation part, which may be due to the presence of nonparabolic-shaped tail states just below the bottom of the original conduction band (**Fig. 4b**). The obtained m^* of 0.1−0.2 m_0 from amorphous IZO is similar to the reported m^* of IZO ($m_d^*/2$ = 0.15 m_0), indicating that m^* does not depend on Zn concentration.[31, 32] This indicates that the Zn 4s orbital-dominated conduction band bottom exhibits a band dispersion similar to that of the In 5s orbital-dominated conduction band bottom.[33] Thus, the addition of Zn to the In_2O_3 films stabilizes the amorphous structure without introducing carrier scattering centers.

Subsequently, we fabricated IZO TFTs with various Zn concentrations and measured their transistor characteristics. **Figure 5a** shows the typical transfer characteristics of the IZO TFTs at room temperature. In all the cases, the channel length (*L*), width (*W*), and applied drain voltage (V_d) were 200 μm, 400 μm, and +5 V, respectively. The subthreshold swing was extracted from V_g, which required an increase in the drain current (I_d) from 1 to 10 pA. The threshold voltage was extracted from the slope and the x-axis intercept of the $I_d^{1/2}$−V_g curve. The threshold voltage (V_{th}) gradually shifted positively (i.e., towards zero) with increasing Zn concentration (**Table 1)**. This is owing

to the reduction in n in the IZO channel. **Figure S1** shows output characteristics of the IZO TFTs with 25% Zn. The I_d showed clear pinch-off behavior and current saturation characteristics at higher V_d.The field effect mobility (μ_{FE}) was calculated from the saturation transfer characteristics at a drain voltage (V_d) of 5 V using the following equation.[34)]

$$\mu_{FE} = \frac{\left(d\sqrt{I_d}/dV_g\right)^2}{(W/2L)C_i}, \qquad \text{(Equation 4)}$$

where C_i is the oxide capacitance of the gate insulator (70 nF cm^{-2} for AlO_x). **Fig. 5b** shows μ_{FE} as a function of Zn concentration. The μ_{FE} values were extracted from **Figure S2**. The μ_{FE} value of amorphous IZO TFTs is higher than that of TFT with a polycrystalline IZO channel layer due to the suppression of grain boundary scattering. The monotonically decrease of μ_{FE} is consistent with the trend of μ_{Hall} (**Fig. 3b**). The best TFT performance was obtained for the amorphous IZO TFT with Zn concentration of 25% (μ_{FE} = 41 cm^2 V^{-1} s^{-1}, subthreshold swing = 0.10 V dec.$^{-1}$, V_{th} = −1.9 V).

Finally, the effects of Zn on the bias stability of IZO TFTs were investigated. We measured the transfer characteristics after applying a positive gate bias stress (PBS; V_g = +20 V) and a negative gate bias stress (NBS; V_g = −20 V) to the TFTs for up to 5000 s at room temperature in air. **Figure S3** summarize the changes in the transfer characteristics of the IZO TFTs in PBS and NBS. The V_{th} shifts of the IZO TFTs with various Zn concentrations after PBS and NBS treatments for 5000 s are summarized in **Figs. 6a and 6b**. Although the effective stress voltage (V_g–V_{th}) applied to the channel is not constant due to the V_{th} of IZO TFTs varying with Zn concentration (**Table S1**), no correlation was observed between the effective stress voltage and V_{th} shift. In the NBS test (**Fig. 6b**), the V_{th} shifts after NBS was negligible, at less than 0.3 V, regardless of the Zn concentration or crystallinity. In general, absorbed/desorbed gas molecules on the channel surface play an important role in determining the V_{th} instability in oxide TFTs.[35-37)] In the present IZO TFT, it is considered that the Y_2O_3 passivation layer formed on the IZO channel suppresses gas absorption/desorption, thereby reducing the V_{th} shift after NBS. By contrast, after PBS test (**Fig. 6a**), the polycrystalline IZO TFTs with Zn concentration of 9% and 86% showed a large positive V_{th} shift after the PBS (ΔV_{th} = 0.74 V for 9% Zn, ΔV_{th} = 0.8 V for 86% Zn). The V_{th} shift caused by PBS is considered to be mainly due to electron trapping in the channel/insulator. The polycrystalline/insulator interface is believed to have a higher density of interface states compared to the amorphous/insulator

interface. In the case of IGZO, the surface roughness of polycrystalline IGZO annealed at 600 °C is over 4 nm, which is significantly greater than that of amorphous IGZO (<0.4 nm).[38] Degradation of IGZO TFT characteristics (decreased mobility and increased subthreshold swing) has also been reported in polycrystalline IGZO TFTs.[39] These results suggest an increase in the trap state density at the polycrystalline/insulator interface. In our case, the root mean square (RMS) surface roughness of IZO films measured by AFM is 0.36 nm for amorphous IZO (25% Zn) and 0.80 nm (9% Zn) and 0.90 nm (86% Zn) for polycrystalline IZO (**Fig. S4**). Therefore, we consider that electron trapping at the polycrystalline/insulator interface is the main cause of PBS degradation. Thus, it was found that the addition of Zn to In_2O_3 is effective in both enhancing mobility and improving reliability.

4. Conclusions

We studied the carrier electron transport properties of IZO films and IZO TFTs with various Zn concentrations (0%, 9%, 25%, 41%, 68%, and 86%). The IZO films with Zn concentrations ranging from 25% to 68% maintained an amorphous phase even after annealing at 300 °C in air, whereas those with Zn concentrations of 9% and 86% underwent crystallization. The carrier effective mass of the IZO films ranged between 0.1 and 0.2 m_0, regardless of the Zn concentration, confirming that both the In 5s and Zn 4s orbitals contributed to the carrier transport. Amorphous IZO TFTs with 25% Zn exhibited the highest μ_{FE} of 41 $cm^2\ V^{-1}\ s^{-1}$ and excellent reliability. In contrast, polycrystalline IZO TFTs showed a low μ_{FE} <12 $cm^2\ V^{-1}\ s^{-1}$ due to the formation of grain boundaries, and poor reliability after positive gate bias, mostly due to electron trapping at the polycrystalline/insulator interface. Our study reports a method to synthesize In_2O_3 TFTs that show reasonably high μ_{FE} and excellent reliability and are useful for the advancement of oxide TFT.

Acknowledgments

This study was supported by a Grant-in-Aid for Innovative Areas (19H05791) from the Japan Society for the Promotion of Science (JSPS). Y. Magari was supported by a Grant-in-Aid from the JSPS (22K14303). Y. Z. was supported by the National Natural Science Foundation of China (Grant No. 52202242), National Science Foundation of the Jiangsu Higher Education Institutions of China (22KJB430002), and the Start-Up Fund of Jiangsu University (5501310015). A part of this study was supported by the Advanced Research Infrastructure for Materials and Nanotechnology in Japan

(JPMXP1223HK0082) of the Ministry of Education, Culture, Sports, Science, and Technology (MEXT).

Competing financial interests
The authors declare no competing financial interests.

Associated content
Supporting Information is available free of charge via the Internet at XXXXXXX.

Author information
Corresponding Authors
Yusaku Magari − Research Institute for Electronic Science, Hokkaido University, N20W10, Kita, Sapporo 001-0020, Japan
ORCID: orcid.org/0000-0001-9655-4283
Email: magari.yusaku@es.hokudai.ac.jp

Hiromichi Ohta − Research Institute for Electronic Science, Hokkaido University, N20W10, Kita, Sapporo 001-0020, Japan
ORCID: orcid.org/0000-0001-7013-0343
Email: hiromichi.ohta@es.hokudai.ac.jp

Author
Yuzhang Wu − Graduate School of Information Science and Technology, Hokkaido University. N14W9, Kita Sapporo 060-0814, Japan
ORCID: orcid.org/0000-0002-6173-4994

Prashant Ghediya − Research Institute for Electronic Science, Hokkaido University, N20W10, Kita, Sapporo 001-0020, Japan
ORCID: orcid.org/0000-0001-9953-0471

Yuqiao Zhang − Institute of Quantum and Sustainable Technology, Jiangsu University, Zhenjiang 212013, China
ORCID: orcid.org/0000-0001-7579-4923

Yasutaka Matsuo − Research Institute for Electronic Science, Hokkaido University, N20W10, Kita, Sapporo 001-0020, Japan
ORCiD: orcid.org/0000-0002-5071-0284

Author Contributions

Y. W. and P. R. G. fabricated the samples and measured their transistor characteristics and thermopower. Y. Z. analyzed the thermopower. Y. Matsuo fabricated AlO_x gate-insulator films. Y. Magari and H. O. planned and supervised the project. All the authors discussed the results and commented on the manuscript.

REFERENCES

1) K. Nomura, H. Ohta, A. Takagi, T. Kamiya, M. Hirano and H. Hosono, Nature **432**, 488 (2004).
2) T. Kamiya and H. Hosono, NPG Asia Mater. **2**, 15 (2010).
3) E. Fortunato, P. Barquinha and R. Martins, Adv Mater. **24**, 2945 (2012).
4) H. Hosono, Nat. Electron. **1**, 428 (2018).
5) J.Y. Kwon and J.K. Jeong, Semicond. Sci. Technol. **30**, 024002 (2015).
6) Y. Hara, T. Kikuchi, H. Kitagawa, J. Morinaga, H. Ohgami, H. Imai, T. Daitoh and T. Matsuo, J. Soc. Inf. Display. **26**, 169 (2018).
7) H. I., B. J. and M. S., Information Display. **38**, 5 (2022).
8) T. Kim, C.H. Choi, J.S. Hur, D. Ha, B.J. Kuh, Y. Kim, M.H. Cho, S. Kim and J.K. Jeong, Adv Mater. **35**, e2204663 (2023).
9) Y. Magari, T. Kataoka, W. Yeh and M. Furuta, Nat. Commun. **13**, 1078 (2022).
10) J.K. Jeong, H.W. Yang, J.H. Jeong, Y.G. Mo and H.D. Kim, Appl. Phys. Lett. **93**, 123508 (2008).
11) J.C. Park, H.N. Lee and S. Im, ACS Appl Mater Inter. **5**, 6990 (2013).
12) H. Ji, A.Y. Hwang, C.K. Lee, P.S. Yun, J.U. Bae, K.S. Park and J.K. Jeong, IEEE Transactions on Electron Devices **62**, 1195 (2015).
13) Z. Yang, J.W. Yang, T. Meng, M.Y. Qu and Q. Zhang, Mater Lett. **166**, 46 (2016).
14) J.W. Zhao, X.A. Zhang, S. Li, H.W. Zheng, G. Yang and W.F. Zhang, Phys Status Solidi A. **214**, 1 (2017).
15) A. Illiberi, I. Katsouras, S. Gazibegovic, B. Cobb, E. Nekovic, W. van Boekel, C. Frijters, J. Maas, F. Roozeboom, Y. Creyghton, P. Poodt and G. Gelinck, Journal of Vacuum Science & Technology A. **36**, 4 (2018).
16) J.M. Lee, H.J. Lee, J.E. Pi, J.H. Yang, J.H. Lee, S.D. Ahn, S.Y. Kang and J. Moon,

Journal of Vacuum Science & Technology A. **37**, 6 (2019).
17) J. Sheng, T. Hong, D. Kang, Y. Yi, J.H. Lim and J.S. Park, ACS Appl Mater Inter. **11**, 12683 (2019).
18) M.Y. Liu, H. Kim, X.Y. Wang, H.W. Song, K. No and S. Lee, ACS Appl. Electron. Mater. **3**, 2703 (2021).
19) M.H. Cho, C.H. Choi and J.K. Jeong, ACS Appl Mater Inter. **14**, 18646 (2022).
20) Y.K. Liang, J.W. Lin, L.C. Peng, Y.M. Hua, T.T. Chou, C.C. Kei, C.C. Lu, H.Y. Huang, S.H. Yeong, Y.M. Lin, P.T. Liu, E.Y. Chang and C.H. Lin, IEEE Trans. Electron Devices. **70**, 1067 (2023).
21) H. Ohta, S.W. Kim, Y. Mune, T. Mizoguchi, K. Nomura, S. Ohta, T. Nomura, Y. Nakanishi, Y. Ikuhara, M. Hirano, H. Hosono and K. Koumoto, Nat. Mater. **6**, 129-134 (2007).
22) H. Ohta, Y. Sato, T. Kato, S.W. Kim, K. Nomura, Y. Ikuhara and H. Hosono, Nat. Commun. **1**, 118 (2010).
23) A.J. Leenheer, J.D. Perkins, M.F.A.M. van Hest, J.J. Berry, R.P. O'Hayre and D.S. Ginley, Phys. Rev. B **77**, 115215 (2008).
24) S-C. Chang and M. H. Shiao, Microelectronics Journal **38**, 1202-1206 (2007).
25) J. Jia, S. Nakamura and Y. Shigesato, Phys. Status Solidi A **213**, 9 (2016).
26) B. Feng, N.R. Lugg, A. Kumamoto, Y. Ikuhara and N. Shibata, ACS Nano. **11**, 11376 (2017).
27) M.V. Frischbier, H.F. Wardenga, M. Weidner, O. Bierwagen, J. Jia, Y. Shigesato and A. Klein , Thin Solid Films **614**, 62-68 (2016).
28) C.B. Vining, Journal of Applied Physics. **69**, 331 (1991).
29) H. Yang, Y.Q. Zhang, Y. Matsuo, Y. Magari and H. Ohta, ACS Appl. Electron. Mater. **4**, 5081 (2022).
30) P. Ghediya, H. Yang, T. Fujimoto, Y.Q. Zhang, Y. Matsuo, Y. Magari and H. Ohta, J Phys Chem C. **127**, 5 (2023).
31) H. Ohta, R. Huang and Y. Ikuhara, Phys. Stat. Sol. **2**, 3 (2008).
32) J.J. Jia, N. Oka and Y. Shigesato, Journal of Applied Physics. **113**, 16 (2013).
33) M. Orita, H. Ohta, M. Hirano, S. Narushima and H. Hosono, Philosophical magazine. **B 81**, 501 (2021).
34) K. Abe, A. Sato, K. Takahashi, H. Kumomi, T. Kamiya and H. Hosono, Thin Solid Films **559**, 40-43 (2014)
35) J.K. Jeong, H.W. Yang, J.H. Jeong, Y.G. Mo and H.D. Kim, Applied Physics Letters. **93**, 12 (2008).
36) D. Kang, H. Lim, C. Kim, I. Song, J. Park, Y. Park and J. Chung, Applied Physics

Letters. **90**, 19 (2007).
37) J.S. Park, J.K. Jeong, H.J. Chung, Y.G. Mo and H.D. Kim, Applied Physics Letters. **92**, 7 (2008).
38) K. Nomura, A. Takagi, T. Kamiya, H. Ohta, M. Hirano and H. Hosono, Jpn. J. Appl. Phys. **45**, 5B (2006).
39) Y. Hanyu, K. Abe, K. Domen, K. Nomura, H. Hiramatsu, H. Kumomi, H. Hosono and T. Kamiya, Journal of Display Technology **10**, 11 (2014).

Table 1. Threshold voltage and subthreshold swing of the IZO TFTs with varied Zn concentration.

Zn concentration (%)	Threshold voltage (V)	Subthreshold swing (V/decade)
0	–11.0	N.D.
9	–8.6	0.25
25	–1.9	0.10
41	–4.7	0.13
68	–3.0	0.26
86	+0.3	0.11

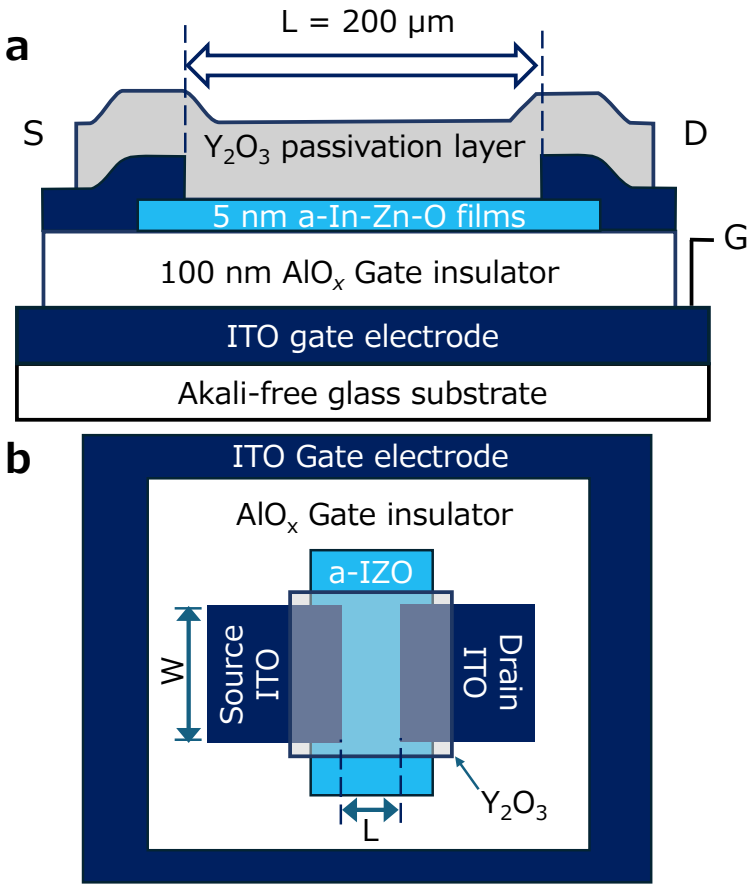

Figure 1. Schematic structure of bottom-gate & top-contact type a-In-Zn-O TFT. (a) cross-sectional schematic image (b) top view of IZO TFT. The width and length of channel layer was 400 μm and 200 μm respectively. The capacitance C_i of the 100-nm AlO_x gate insulator was 70 nF cm^{-2}. A 5-nm IZO channel was covered with a Y_2O_3 passivation layer to prevent gas adsorption/desorption.

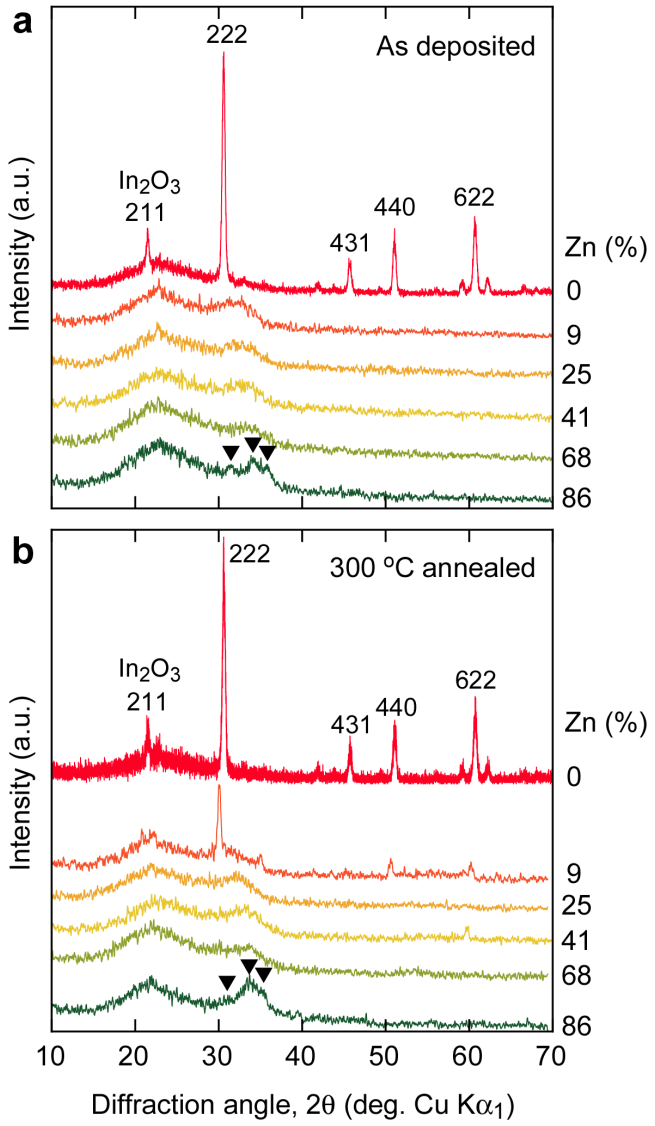

Figure 2. Grazing incident XRD patterns of the resultant IZO films. (a) as-deposited and (b) 300 °C annealed. The incident angle of the X-rays was 0.5°. In_2O_3 film with and without annealing shows intense diffraction peaks. For Zn concentration of 25%−68%, a halo is seen at 2θ ~34°, whereas diffraction peaks appear for Zn concentration of 9% and 86% (triangles), especially after annealing. IZO films with a Zn concentration of 25%−68% maintain an amorphous structure even after annealing at 300 °C.

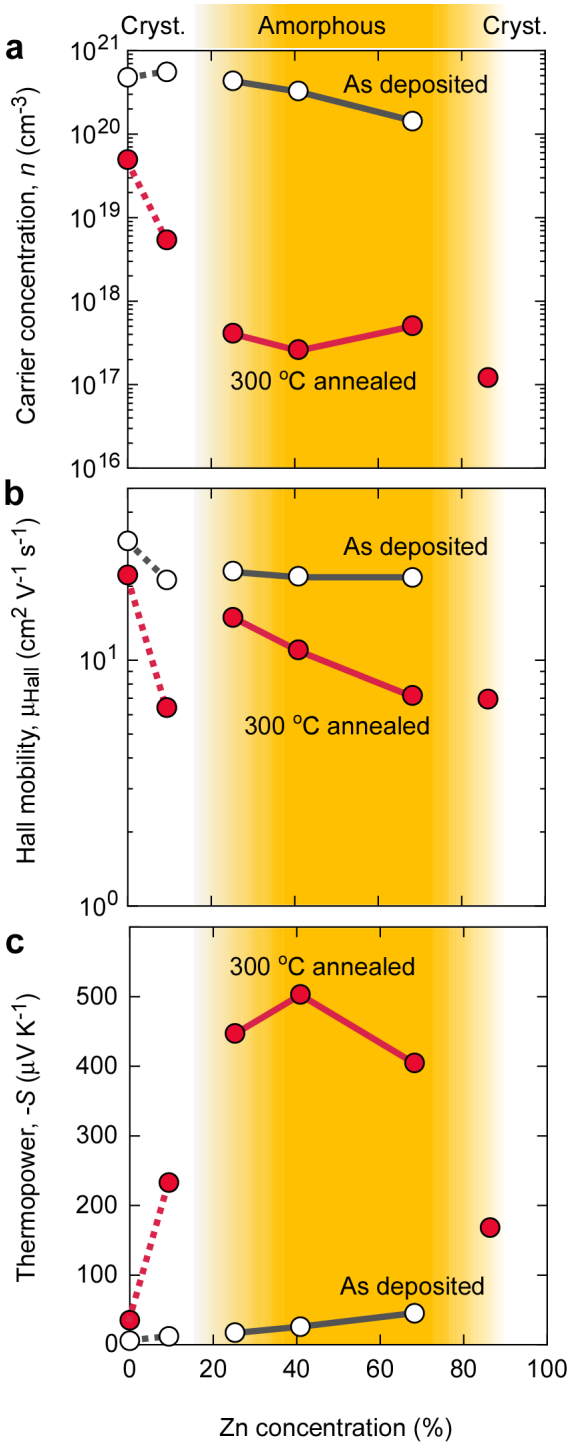

Figure 3. **Electron transport properties of the IZO films at room temperature.** (a) Carrier concentration (n), (b) Hall mobility (μ_{Hall}), and thermopower (S) of the IZO films. After annealing, the n of amorphous IZO films with a Zn concentration of 25%−86% show low n ($<10^{18}$ cm^{-3}). The amorphous IZO films showed higher μ_{Hall} than that of polycrystalline films except for the In_2O_3 film (Zn 0%).

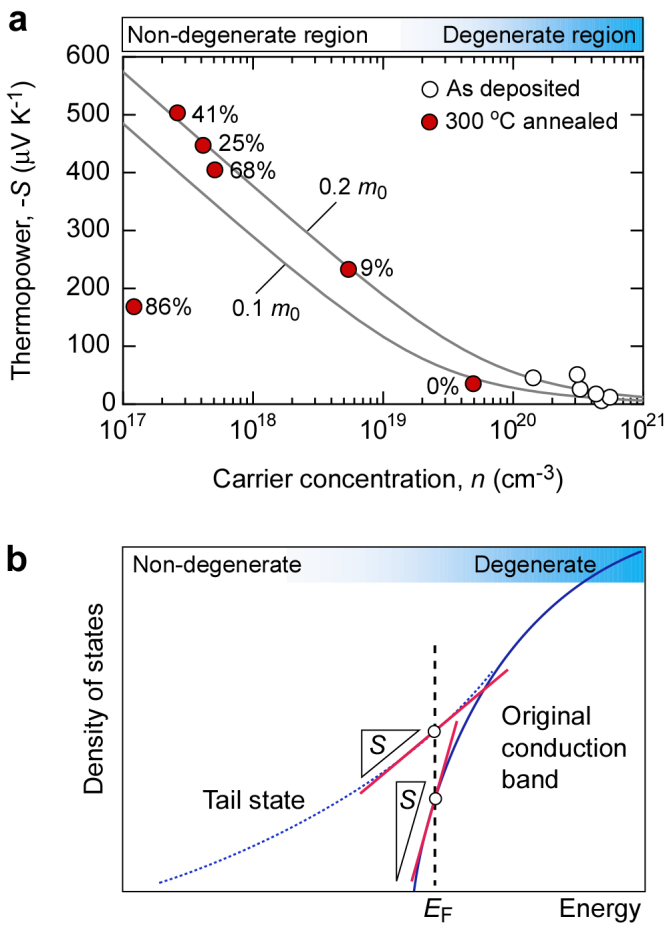

Figure 4. **Thermopower of the IZO films with various Zn concentrations.** *S*–log *n* plot of the IZO films with various Zn concentrations. The *m** of IZO films, except for the Zn concentration of 86%, lies between 0.1 and 0.2 m_0. (b) Schematic energy dependence of the density of states around the conduction band minimum of the IZO films. Since the *S* reflects the energy derivative of the density of states at the Fermi energy (E_F), the observable *S* of the semiconductor with a non-parabolic tail state is smaller than that of the parabolic density of states.

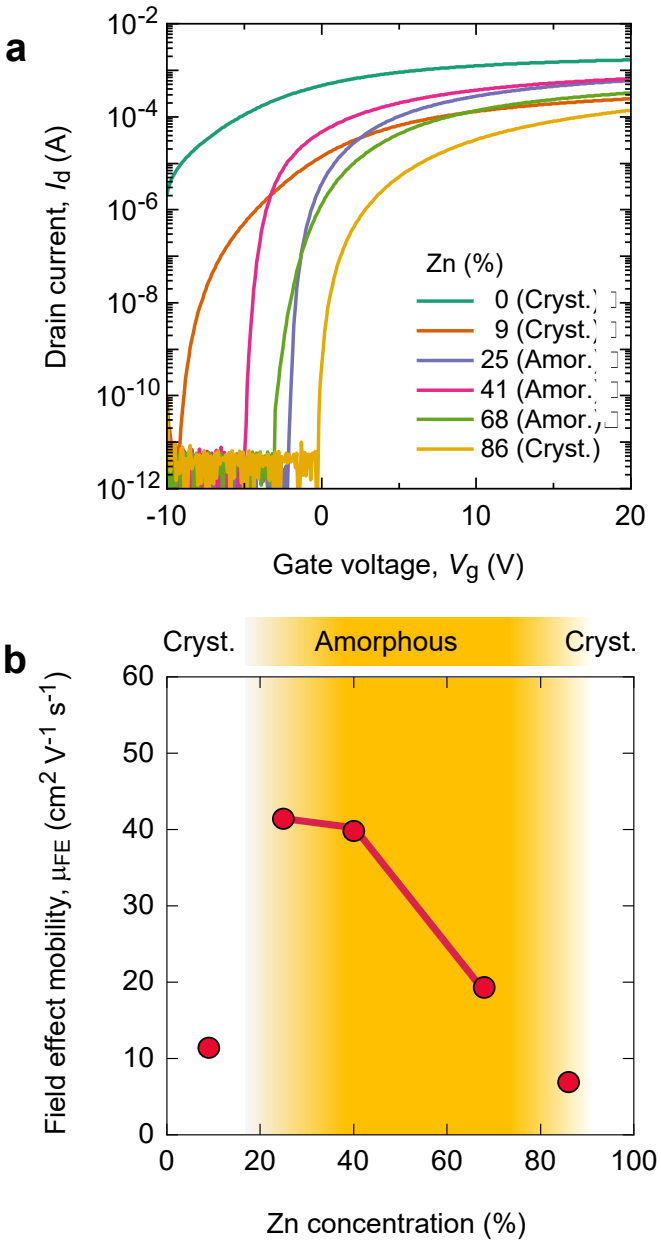

Figure 5. **Typical transistor characteristics of the IZO TFTs at room temperature.** (a) Transfer characteristics (L = 200 μm, W = 400 μm, V_d = +5 V). The threshold voltage gradually shifts positively (i.e., towards zero) with increasing Zn concentration. (b) Field effect mobility (μ_{FE}) of the IZO TFTs. Amorphous IZO TFTs show higher μ_{FE} than that of polycrystalline In_2O_3 and IZO TFTs. The highest μ_{FE} is ~41 $cm^2 V^{-1} s^{-1}$, which is obtained for 25% Zn.

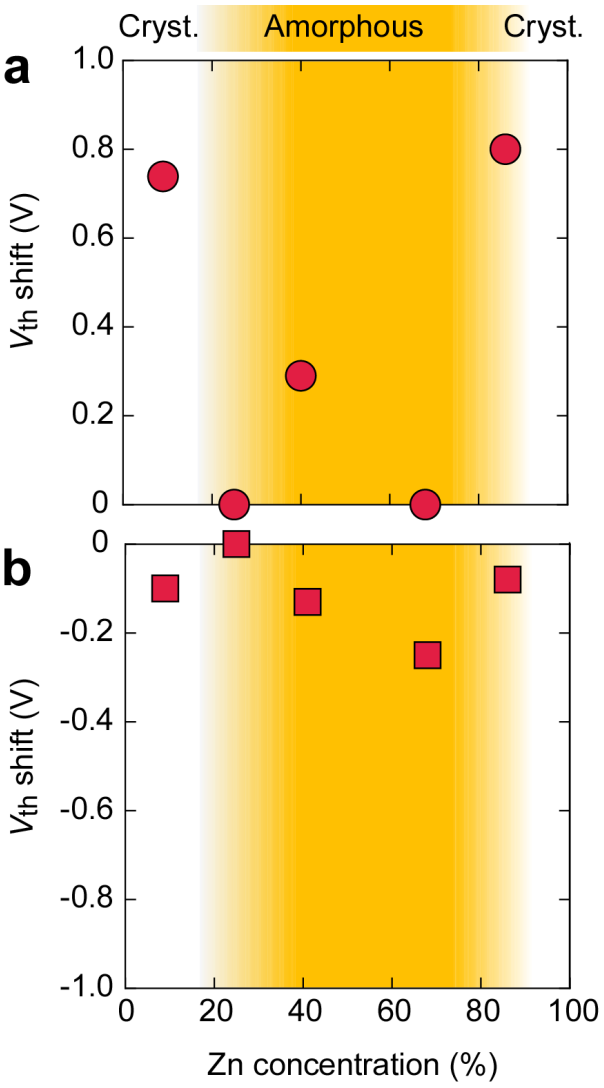

Figure 6. Reliability of the IZO TFTs with different Zn concentrations. (a,b) V_{th} shifts of the IZO TFTs with various Zn concentrations after the application of (a) PBS and (b) NBS for 5000 s. The IZO TFT with 25% Zn shows a small V_{th} shift after the application of the PBS and NBS. Amorphous IZO (Zn concentration 25%−86%) TFTs show small V_{th} shifts after PBS compared to that of polycrystalline IZO TFTs.

Supplementary Information

High-mobility and High-reliability Zn-incorporated Amorphous In_2O_3-based Thin-Film Transistors

Yuzhang Wu[1], Yusaku Magari[2,*], Prashant R. Ghediya[2], Yuqiao Zhang[3], Yasutaka Matsuo[2], and Hiromichi Ohta[2,*]

[1] *Graduate School of Information Science and Technology, Hokkaido University. N14W9, Kita Sapporo 060-0814, Japan*
[2] *Research Institute for Electronic Science, Hokkaido University, N20W10, Kita, Sapporo 001-0020, Japan*
[3] *Institute of Quantum and Sustainable Technology, Jiangsu University, Zhenjiang 212013, China*
*Email: magari.yusaku@es.hokudai.ac.jp, hiromichi.ohta@es.hokudai.ac.jp

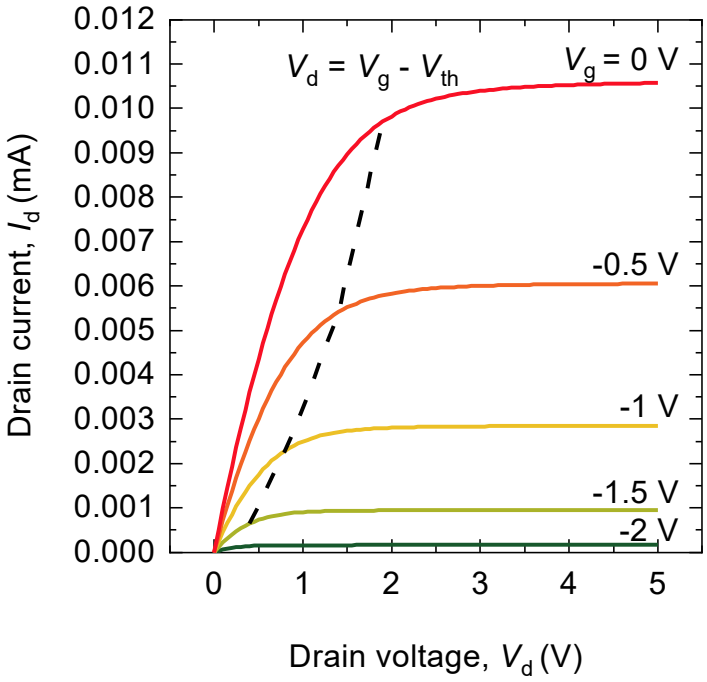

Figure S1. Output characteristics of the IZO TFTs with 25% Zn. The I_d showed clear pinch-off behavior and current saturation characteristics at higher V_d.

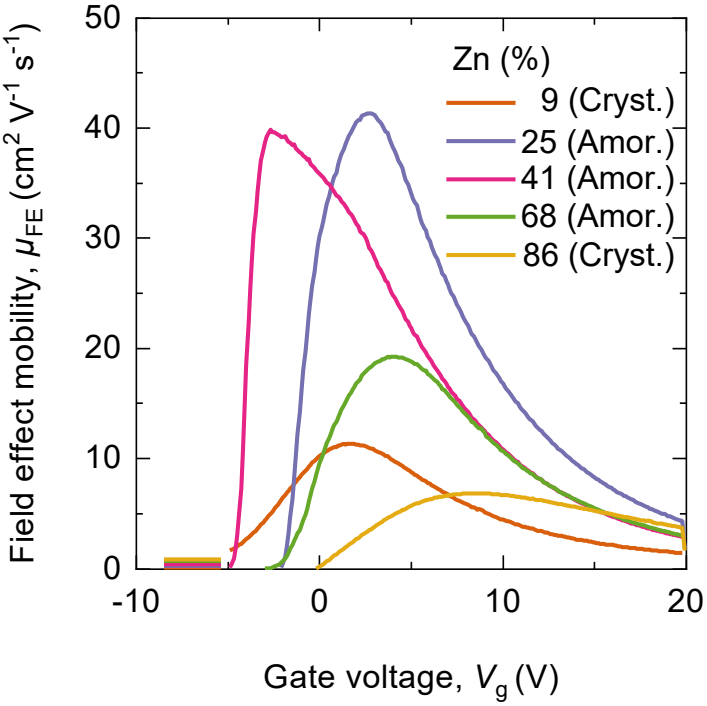

Figure S2. Relationship between μ_{FE} and V_g in IZO TFTs with various Zn concentrations.

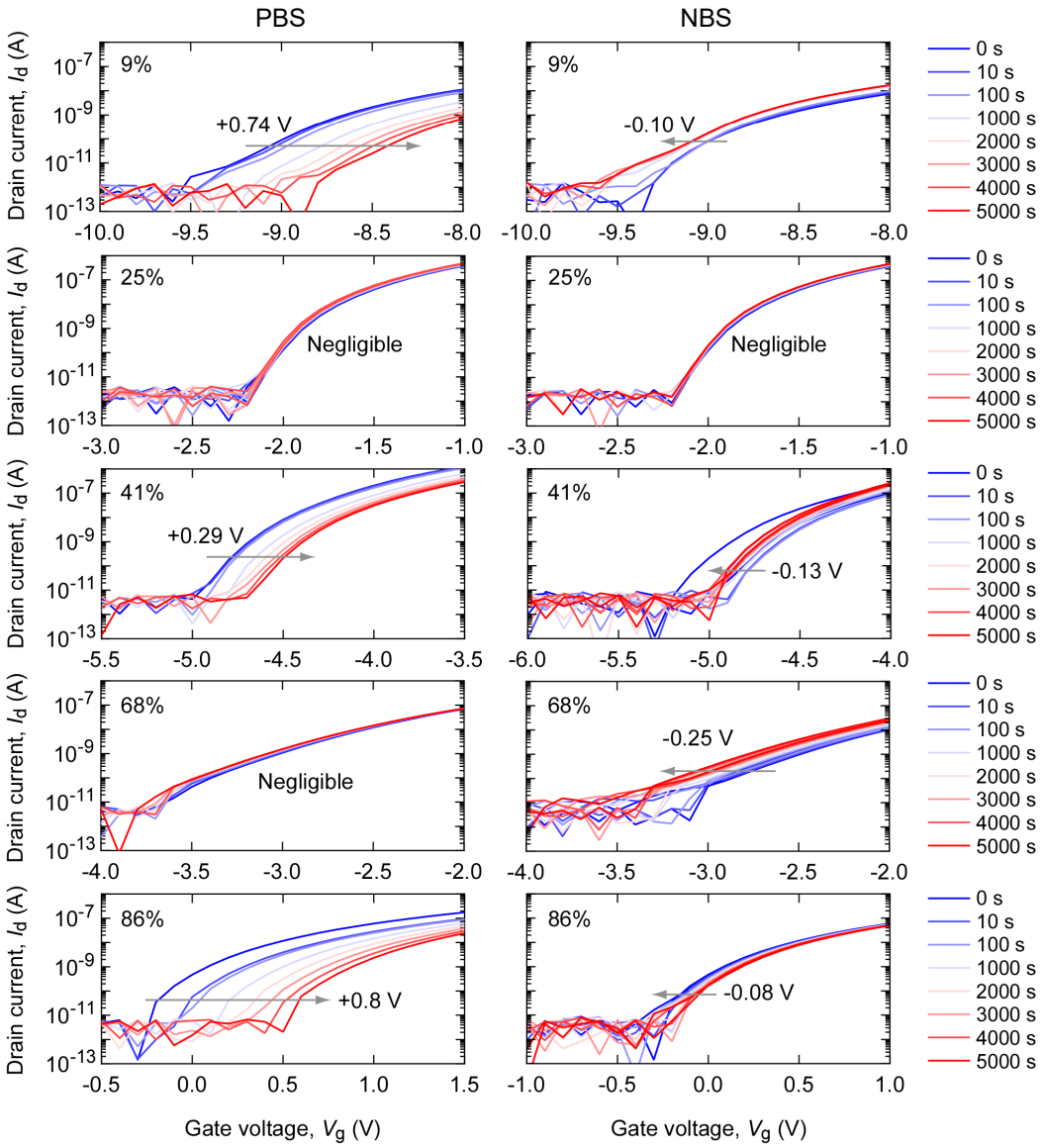

Figure S3. Change in the transfer characteristics of the IZO TFTs under PBS (V_g =+20 V) and NBS (V_g =−20 V). The surface of the channel was passivated using a Y_2O_3 thin film.

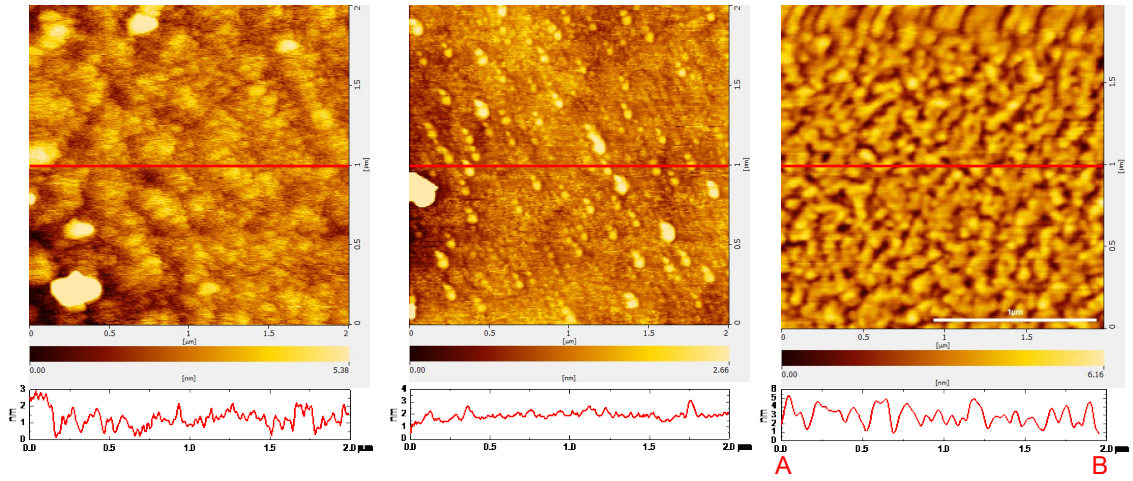

Figure S4. AFM images of IZO films with (a) 9% Zn, (b) 25% Zn, and (c) 86% Zn after annealing at 300 °C. The root mean square (RMS) values of amorphous IZO (25% Zn) is samaller than that of polycrystalline IZO films (9% and 86% Zn).

Table S1. Bias voltage of PBS and NBS applying on channel layer with varied Zn concentration.

Zn concentration (%)	V_g–V_{th} (PBS) (V)	V_g–V_{th} (NBS) (V)
9	28.6	–11.4
25	21.9	–18.1
41	24.7	–15.3
68	23.0	–17.0
86	19.7	–20.3